

# Dynamic Anti-plane Behavior of Piezoelectric Medium with a Cylindrical Inclusion in Right-angle Field

Dong Li<sup>1</sup>, Huicong Wang<sup>2\*</sup>, Yaping Liu<sup>3</sup>

<sup>1</sup>Center for Quality Management, Hebei JiaoTong Vocational and Technical College, Shijiazhuang, Hebei, 050035, People's Republic of China

<sup>2</sup>Department of Road and Bridge Engineering, Hebei Jiaotong Vocational and Technical College, Shijiazhuang, Hebei, 050091, People's Republic of China

<sup>3</sup>Department of Rail Transit, Shijiazhuang, Hebei Jiaotong Vocational and Technical College, Hebei, 050035, People's Republic of China

\*Corresponding author.

## **Abstract:**

Based on the complex variables and the mirror imaging methods, the dynamic anti-plane behavior of right-angle piezoelectric medium with a single cylindrical inclusion is studied. The analytical expressions of dynamic stress concentration factor (DSCF) and electric field intensity concentration factor (EFICF) at the inclusion in right-angle piezoelectric medium under the scattering of anti-plane shear waves are obtained, and the calculation results under different parameter combinations are plotted. The results indicate that the DSCFs and EFICFs around the inclusion is closely related to the frequency of incident wave, physical parameters of material and geometric parameters of structure.

**Keywords:** *Right-Angle piezoelectric medium, Cylindrical inclusion, Dynamic stress concentration factor, Electric field intensity concentration factor.*

---

## I. INTRODUCTION

Piezoelectric materials will inevitably produce defects such as holes or inclusions during manufacturing, and the structure often fracture or fail because of the stress concentration near the defects in the use process. Therefore, studying the failure mechanism of such problems has become an important topic for researchers.

Recent years, in the research of static fracture, Zhao [1], Gao [2-3], Lee [4], Sosa [5] and other scholars studied the field concentration around the hole in piezoelectric materials under

the action of infinite load. Suzuki [6-7], Chen [8], Eugene Pak [9], Yang [10], Meguid [11] and Hu [12] analyzed the plane shear load and in-plane electric load of piezoelectric materials with inclusions. In the dynamic fracture field, Shindo et al. [13] studied the dynamic behavior of an infinite piezoelectric medium with cylindrical piezoelectric inclusions under the action of time-harmonic shear waves and steady-state in-plane electric loads; Du et al. [14] and Feng et al. [15] investigated the scattering of SH waves by partially debonded cylindrical inclusions in piezoelectric materials.

It is found that, compared with the static fracture research, there is less research on dynamic fracture mechanics of piezoelectric materials with inclusion defects, and most of the analysis are simplified to the problem of infinite field or semi-infinite field model. And the dynamic fracture mechanics model of piezoelectric structures in angular field has not been further discussed because of its complexity. In the present paper, the dynamic anti-plane behavior of right-angle piezoelectric medium, which contain a single cylindrical inclusion, are studied under the incident anti-plane shearing wave. It can be provided an effective theoretical analysis method for this kind of problem.

## II. FUNDAMENTAL EQUATIONS

In transversely isotropic piezoelectric media, it is assumed that the  $Z$  axis is the electric polarization direction and the  $x$ - $y$  is the isotropic plane of the material. When the physical force and free charge are zero, the equilibrium equation of the steady-state anti-plane dynamics problem is:

$$\begin{aligned} c_{44}\nabla^2 w + e_{15}\nabla^2 \phi + \rho\omega^2 w &= 0 \\ e_{15}\nabla^2 w - \kappa_{11}\nabla^2 \phi &= 0 \end{aligned} \quad (1)$$

Where  $w$ ,  $\rho$ ,  $\omega$  and  $\phi$  are anti-plane displacement, mass density, frequency of the incident wave and electric potential, respectively; while  $c_{44}$  is the shear elastic modulus,  $e_{15}$  is the piezoelectric constant, and  $\kappa_{11}$  is the dielectric constant of the medium, respectively.

A new function  $\varphi(x, y)$  [16] is introduced, which satisfies the equation,

$$\varphi = \phi - \frac{e_{15}}{\kappa_{11}} w \quad (2)$$

By substituting equation (2) into equation (1), the control equation can be simplified as:

$$\nabla^2 w + k^2 w = 0, \quad \nabla^2 \varphi = 0 \quad (3)$$

Wherein,  $\nabla^2$  is the laplace operator,  $\nabla^2 = \frac{\partial^2}{\partial x^2} + \frac{\partial^2}{\partial y^2}$ ;  $k$  is the wave number,  $k^2 = \frac{\rho \omega^2}{c^*}$ , and  $c^* = c_{44} + \frac{e_{15}^2}{\kappa_{11}} = c_{44}(1 + \lambda)$ .

Introducing a complex variables  $\eta = x + iy$  and its conjugate  $\bar{\eta} = x - iy$ , the governing equations and constitutive laws on complex planes  $\eta = re^{i\theta}$  and  $\bar{\eta} = re^{-i\theta}$  can be written as follows:

$$\frac{\partial^2 w}{\partial \eta \partial \bar{\eta}} + \frac{1}{4} k^2 w = 0, \quad \frac{\partial^2 \varphi}{\partial \eta \partial \bar{\eta}} = 0 \quad (4)$$

$$\begin{aligned} \tau_{rz} &= c_{44} \left( \frac{\partial w}{\partial \eta} e^{i\theta} + \frac{\partial w}{\partial \bar{\eta}} e^{-i\theta} \right) + e_{15} \left( \frac{\partial \phi}{\partial \eta} e^{i\theta} + \frac{\partial \phi}{\partial \bar{\eta}} e^{-i\theta} \right) \\ \tau_{\theta z} &= ic_{44} \left( \frac{\partial w}{\partial \eta} e^{i\theta} - \frac{\partial w}{\partial \bar{\eta}} e^{-i\theta} \right) + ie_{15} \left( \frac{\partial \phi}{\partial \eta} e^{i\theta} - \frac{\partial \phi}{\partial \bar{\eta}} e^{-i\theta} \right) \\ D_r &= e_{15} \left( \frac{\partial w}{\partial \eta} e^{i\theta} + \frac{\partial w}{\partial \bar{\eta}} e^{-i\theta} \right) - \kappa_{11} \left( \frac{\partial \phi}{\partial \eta} e^{i\theta} + \frac{\partial \phi}{\partial \bar{\eta}} e^{-i\theta} \right) \\ D_\theta &= ie_{15} \left( \frac{\partial w}{\partial \eta} e^{i\theta} - \frac{\partial w}{\partial \bar{\eta}} e^{-i\theta} \right) - i\kappa_{11} \left( \frac{\partial \phi}{\partial \eta} e^{i\theta} - \frac{\partial \phi}{\partial \bar{\eta}} e^{-i\theta} \right) \end{aligned} \quad (5)$$

Where  $\tau_{rz}$  and  $\tau_{\theta z}$  are shear stress components;  $D_r$  and  $D_\theta$  are electric displacement components.

### III. PHYSICAL MODEL OF THE PROBLEM

The mechanical model of the right-angle piezoelectric material with a single cylindrical elastic conductive inclusion is shown in Figure 1. The radius of the inclusion is  $R$ , and the distance between the inclusion center and the two right-angle boundary surfaces  $h$  and  $d$  respectively. A steady state SH-wave is incident at the angle  $\alpha_0$  with the horizontal direction. The boundary conditions of the problem can be written as:

$$\begin{aligned}
 \Gamma_H: \tau_{yz}^M = 0, D_y^M = 0 \quad (y = h) \\
 \Gamma_V: \tau_{xz}^M = 0, D_x^M = 0 \quad (x = -d) \\
 \Gamma_R: w^M = w^I, \tau_{rz}^M = \tau_{rz}^I, D_r^M = D_r^I, \phi^M = \phi^I \quad (r = R)
 \end{aligned}
 \tag{6}$$

Wherein, the superscript "M" represents the physical quantity in the matrix and "I" represents the physical quantity in the inclusion.

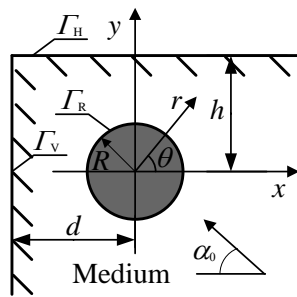


Fig 1: model of a right-angle plane with a single cylindrical elastic conductive inclusion

#### IV. THEORETICAL ANALYSIS

The solutions satisfying the governing equations under the constraint of boundary conditions should include two parts, namely, the field generated by the disturbance of incident wave and the scattering field excited by the inclusion.

The incident displacement field  $w^{(i)}$  and the potential field  $\phi^{(i)}$  in the right-angle field can be expressed as:

$$w^{(i)} = w_0 \exp \left\{ \frac{ik}{2} \cdot [(\eta - ih)e^{-i\beta_0} + (\bar{\eta} + ih)e^{i\beta_0}] \right\}, \quad \phi^{(i)} = \frac{e_{15}}{\kappa_{11}} \cdot w^{(i)}
 \tag{7}$$

Where  $w_0$  is the amplitude of the incident wave,  $\beta_0 = \pi - \alpha_0$

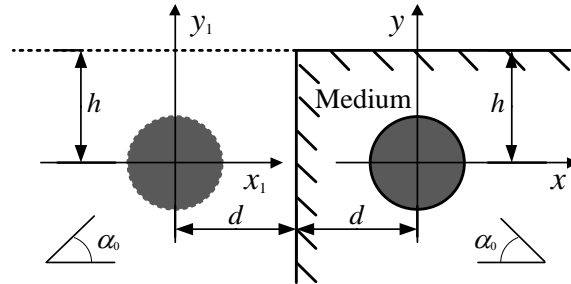


Fig 2: the semi-infinite space mirrored by the right-angle plane

The scattering fields generated by the cylindrical inclusion is symmetrical, so the right-angle field model can be mirrored into a semi-infinite piezoelectric medium space by the mirror imaging methods [17]. The equivalent displacement field expression  $w^{(ie)}$  and potential field expression  $\phi^{(ie)}$  which meet the boundary conditions can be written as:

$$w^{(ie)} = w_0 \cdot (T_1 + T_2), \quad \phi^{(ie)} = \frac{e_{15}}{\kappa_{11}} \cdot w^{(ie)} \quad (8)$$

The equivalent reflection displacement field expression  $w^{(re)}$  and potential field expression  $\phi^{(re)}$  in the semi-infinite space can be written as:

$$w^{(re)} = w_0 \cdot (T_3 + T_4), \quad \phi^{(re)} = \frac{e_{15}}{\kappa_{11}} \cdot w^{(re)} \quad (9)$$

Wherein,  $\eta_1 = \eta + 2d$ ,  $\bar{\eta}_1 = \bar{\eta} + 2d$

$$T_1 = \exp\left\{\frac{ik}{2} \cdot [(\eta - ih)e^{-i\beta_0} + (\bar{\eta} + ih)e^{i\beta_0}]\right\}, \quad T_2 = \exp\left\{\frac{ik}{2} \cdot [(\eta_1 - ih)e^{-i\alpha_0} + (\bar{\eta}_1 + ih)e^{i\alpha_0}]\right\}$$

$$T_3 = \exp\left\{\frac{ik}{2} \cdot [(\eta - ih)e^{i\beta_0} + (\bar{\eta} + ih)e^{-i\beta_0}]\right\}, \quad T_4 = \exp\left\{\frac{ik}{2} \cdot [(\eta_1 - ih)e^{i\alpha_0} + (\bar{\eta}_1 + ih)e^{-i\alpha_0}]\right\}$$

The scattering displacement field  $w^{(s)}$  and the potential field  $\phi^{(s)}$ , which meet the boundary conditions on two right-angle edges, can be expressed as:

$$w^{(s)} = \sum_{n=-\infty}^{\infty} A_n \sum_{j=1}^4 S_n^{(j)}, \quad \phi^{(s)} = \frac{e_{15}}{\kappa_{11}} \cdot w^{(s)} + f^{(s)} \quad (10)$$

Wherein,

$$\begin{cases} S_n^{(1)} = H_n^{(1)}(k|\eta|)[\eta/|\eta|]^n, & S_n^{(2)} = H_n^{(1)}(k|\eta-2ih|)[(\eta-2ih)/|\eta-2ih|]^{-n} \\ S_n^{(3)} = (-1)^n H_n^{(1)}(k|\eta_1|)[\eta_1/|\eta_1|]^{-n}, & S_n^{(4)} = (-1)^n H_n^{(1)}(k|\eta_1-2ih|)[(\eta_1-2ih)/|\eta_1-2ih|]^n \end{cases}$$

The expression of  $f^{(s)}$  is:

$$f^{(s)} = \sum_{n=1}^{\infty} D_n P_n^{(1)} + \sum_{n=1}^{\infty} E_n P_n^{(2)} \quad (11)$$

Wherein,

$$\begin{aligned} P_n^{(1)} &= \eta^{-n} + (\bar{\eta} + 2ih)^{-n} + (-1)^n (\eta_1 - 2ih)^{-n} + (-1)^n \bar{\eta}_1^{-n} \\ P_n^{(2)} &= \bar{\eta}^{-n} + (\eta - 2ih)^{-n} + (-1)^n \eta_1^{-n} + (-1)^n (\bar{\eta}_1 + 2ih)^{-n} \end{aligned}$$

Where  $A_n$ ,  $D_n$  and  $E_n$  are unknown constants, while  $H_n^{(1)}(*)$  is the Hankel function of the first kind.

According to the elastic dynamic theory, the displacement field inside the elastic inclusion is expressed as follows:

$$w^I = \sum_{n=-\infty}^{+\infty} F_n \cdot J_n(k^I|\eta|) \cdot \left(\frac{\eta}{|\eta|}\right)^n \quad (12)$$

The potential field inside the inclusion should be finite and satisfy the governing equation  $\nabla^2 \phi^I = 0$ :

$$\begin{aligned} \phi^I &= \frac{\epsilon_{15}^I}{\kappa_{11}^I} \cdot w^I + f^I \\ f^I &= \sum_{n=0}^{+\infty} L_n \eta^n + \sum_{n=1}^{+\infty} M_n \bar{\eta}^n \end{aligned} \tag{13}$$

Where  $F_n, L_n$  and  $M_n$  are unknown constants.

It can be obtained from the third equation in the boundary condition (6):

$$\begin{cases} w^{(ie)} + w^{(re)} + w^{(s)} = w^I \\ \tau_{rz}^{(ie)} + \tau_{rz}^{(re)} + \tau_{rz}^{(s)} = \tau_{rz}^I \\ \phi^{(ie)} + \phi^{(re)} + \phi^{(s)} = \phi^I \\ D_r^{(ie)} + D_r^{(re)} + D_r^{(s)} = D_r^I \end{cases} \quad (r = R) \tag{14}$$

The infinite algebraic equations for determining the unknown constants  $A_n, D_n, E_n, F_n, L_n$  and  $M_n$  can be obtained from the equation (14):

$$\begin{aligned} \sum_{n=-\infty}^{\infty} A_n \zeta_n^{(11)} + \sum_{n=-\infty}^{\infty} F_n \zeta_n^{(14)} &= \zeta^{(1)} \\ \sum_{n=-\infty}^{\infty} A_n \zeta_n^{(21)} + \sum_{n=1}^{\infty} D_n \zeta_n^{(22)} + \sum_{n=1}^{\infty} E_n \zeta_n^{(23)} + \sum_{n=-\infty}^{\infty} F_n \zeta_n^{(24)} + \sum_{n=0}^{\infty} L_n \zeta_n^{(25)} + \sum_{n=1}^{\infty} M_n \zeta_n^{(26)} &= \zeta^{(2)} \\ \sum_{n=-\infty}^{\infty} A_n \zeta_n^{(31)} + \sum_{n=1}^{\infty} D_n \zeta_n^{(32)} + \sum_{n=1}^{\infty} E_n \zeta_n^{(33)} + \sum_{n=-\infty}^{\infty} F_n \zeta_n^{(34)} + \sum_{n=0}^{\infty} L_n \zeta_n^{(35)} + \sum_{n=1}^{\infty} M_n \zeta_n^{(36)} &= \zeta^{(3)} \\ \sum_{n=1}^{\infty} D_n \zeta_n^{(42)} + \sum_{n=1}^{\infty} E_n \zeta_n^{(43)} + \sum_{n=1}^{\infty} L_n \zeta_n^{(45)} + \sum_{n=1}^{\infty} M_n \zeta_n^{(46)} &= \zeta^{(4)} \end{aligned} \tag{15}$$

Where,

$$\zeta_n^{(11)} = \sum_{j=1}^4 S_n^{(j)}, \quad \zeta_n^{(14)} = -J_n(k_{II}|\eta|) \cdot \left(\frac{\eta}{|\eta|}\right)^n$$

$$\xi_n^{(21)} = \frac{k^M}{2} c_{44}^M (1 + \lambda^M) \cdot \left[ \sum_{j=1}^4 \chi_n^{(j)} \exp(i\theta) + \sum_{j=1}^4 \gamma_n^{(j)} \exp(-i\theta) \right]$$

$$\xi_n^{(22)} = e_{15}^M \left[ \sum_{j=1}^2 \zeta_n^{(j)} \exp(i\theta) + \sum_{j=1}^2 \mathcal{G}_n^{(j)} \exp(-i\theta) \right], \quad \xi_n^{(23)} = e_{15}^M \left[ \sum_{j=1}^2 \upsilon_n^{(j)} \exp(i\theta) + \sum_{j=1}^2 \psi_n^{(j)} \exp(-i\theta) \right]$$

$$\xi_n^{(24)} = -\frac{k^I}{2} c_{44}^I (1 + \lambda^I) \cdot \left[ J_{n-1}(k^I |\eta|) \cdot \left( \frac{\eta}{|\eta|} \right)^{n-1} \exp(i\theta) - J_{n+1}(k^I |\eta|) \cdot \left( \frac{\eta}{|\eta|} \right)^{n+1} \exp(-i\theta) \right]$$

$$\xi_n^{(25)} = -e_{15}^I \cdot n \cdot \eta^{n-1} \exp(i\theta), \quad \xi_n^{(26)} = -e_{15}^I \cdot n \cdot \bar{\eta}^{n-1} \exp(-i\theta)$$

$$\xi_n^{(31)} = \frac{e_{15}^M}{\kappa_{11}^M} \cdot \sum_{j=1}^4 S_n^{(j)}$$

$$\xi_n^{(32)} = \eta^{-n} + (\bar{\eta} + 2ih)^{-n} + (-1)^n (\eta_1 - 2ih)^{-n} + (-1)^n \bar{\eta}_1^{-n}$$

$$\xi_n^{(33)} = \bar{\eta}^{-n} + (\eta - 2ih)^{-n} + (-1)^n \eta_1^{-n} + (-1)^n (\bar{\eta}_1 + 2ih)^{-n}$$

$$\xi_n^{(34)} = -\frac{e_{15}^I}{\kappa_{11}^I} \cdot J_n(k^I |\eta|) \cdot \left( \frac{\eta}{|\eta|} \right)^n, \quad \xi_n^{(35)} = -\eta^n, \quad \xi_n^{(36)} = -\bar{\eta}^n$$

$$\xi_n^{(42)} = \kappa_{11}^M \cdot \left[ \sum_{j=1}^2 \zeta_n^{(j)} \exp(i\theta) + \sum_{j=1}^2 \mathcal{G}_n^{(j)} \exp(-i\theta) \right]$$

$$\xi_n^{(43)} = \kappa_{11}^M \cdot \left[ \sum_{j=1}^2 \upsilon_n^{(j)} \exp(i\theta) + \sum_{j=1}^2 \psi_n^{(j)} \exp(-i\theta) \right]$$

$$\xi_n^{(45)} = -\kappa_{11}^I \cdot n \cdot \eta^{n-1} \exp(i\theta), \quad \xi_n^{(46)} = -\kappa_{11}^I \cdot n \cdot \bar{\eta}^{n-1} \exp(-i\theta)$$

$$\zeta^{(1)} = -w_0 [T_1 + T_2 + T_3 + T_4]$$

$$\zeta^{(2)} = -ic_{44}^M (1 + \lambda^M) k^M w_0 [T_1 \cos(\theta - \beta_0) + T_2 \cos(\theta - \alpha_0) + T_3 \cos(\theta + \beta_0) + T_4 \cos(\theta + \alpha_0)]$$

$$\zeta^{(3)} = -\frac{e_{15}^M}{\kappa_{11}^M} \cdot w_0 \cdot [T_1 + T_2 + T_3 + T_4], \quad \zeta^{(4)} = 0$$

$$\left\{ \begin{aligned} \chi_n^{(1)} &= H_{n-1}^{(1)}(k^M |\eta|) \left( \frac{\eta}{|\eta|} \right)^{n-1}, & \chi_n^{(2)} &= -H_{n+1}^{(1)}(k^M |\eta - 2ih|) \left( \frac{\eta - 2ih}{|\eta - 2ih|} \right)^{-(n+1)} \\ \chi_n^{(3)} &= -(-1)^n H_{n+1}^{(1)}(k^M |\eta_1|) \left( \frac{\eta_1}{|\eta_1|} \right)^{-(n+1)}, & \chi_n^{(4)} &= (-1)^n H_{n-1}^{(1)}(k^M |\eta_1 - 2ih|) \left( \frac{\eta_1 - 2ih}{|\eta_1 - 2ih|} \right)^{n-1} \end{aligned} \right.$$

$$\left\{ \begin{aligned} \gamma_n^{(1)} &= -H_{n+1}^{(1)}(k^M |\eta|) \left( \frac{\eta}{|\eta|} \right)^{n+1}, & \gamma_n^{(2)} &= H_{n-1}^{(1)}(k^M |\eta - 2ih|) \left( \frac{\eta - 2ih}{|\eta - 2ih|} \right)^{-(n-1)} \\ \gamma_n^{(3)} &= (-1)^n H_{n-1}^{(1)}(k^M |\eta_1|) \left( \frac{\eta_1}{|\eta_1|} \right)^{-(n-1)}, & \gamma_n^{(4)} &= -(-1)^n H_{n+1}^{(1)}(k^M |\eta_1 - 2ih|) \left( \frac{\eta_1 - 2ih}{|\eta_1 - 2ih|} \right)^{n+1} \end{aligned} \right.$$

$$\begin{cases} \zeta_n^{(1)} = (-n) \cdot \eta^{-(n+1)}, & \zeta_n^{(2)} = (-1)^{n+1} \cdot n(\eta_1 - 2ih)^{-(n+1)} \\ \mathcal{G}_n^{(1)} = (-n) \cdot (\bar{\eta} + 2ih)^{-(n+1)}, & \mathcal{G}_n^{(2)} = (-1)^{n+1} \cdot n\bar{\eta}_1^{-(n+1)} \\ \mathcal{V}_n^{(1)} = (-n) \cdot (\eta - 2ih)^{-(n+1)}, & \mathcal{V}_n^{(2)} = (-1)^{n+1} \cdot n\eta_1^{-(n+1)} \\ \psi_n^{(1)} = (-n) \cdot \bar{\eta}^{-(n+1)}, & \psi_n^{(2)} = (-1)^{n+1} \cdot n(\bar{\eta}_1 + 2ih)^{-(n+1)} \end{cases}$$

$$\left\{ \begin{aligned} T_1 &= \exp \left\{ \frac{ik^M}{2} \cdot [(\eta - ih)e^{-i\beta_0} + (\bar{\eta} + ih)e^{i\beta_0}] \right\}, & T_2 &= \exp \left\{ \frac{ik^M}{2} \cdot [(\eta_1 - ih)e^{-i\alpha_0} + (\bar{\eta}_1 + ih)e^{i\alpha_0}] \right\} \\ T_3 &= \exp \left\{ \frac{ik^M}{2} \cdot [(\eta - ih)e^{i\beta_0} + (\bar{\eta} + ih)e^{-i\beta_0}] \right\}, & T_4 &= \exp \left\{ \frac{ik^M}{2} \cdot [(\eta_1 - ih)e^{i\alpha_0} + (\bar{\eta}_1 + ih)e^{-i\alpha_0}] \right\} \end{aligned} \right\}$$

Both sides of equation (15) are multiplied by  $e^{-im\theta}$  and integrated on  $(-\pi, \pi)$ :

$$\begin{aligned} \sum_{n=-\infty}^{\infty} A_n \zeta_{mn}^{(11)} + \sum_{n=-\infty}^{\infty} F_n \zeta_{mn}^{(14)} &= \zeta_m^{(1)} \\ \sum_{n=-\infty}^{\infty} A_n \zeta_{mn}^{(21)} + \sum_{n=1}^{\infty} D_n \zeta_{mn}^{(22)} + \sum_{n=1}^{\infty} E_n \zeta_{mn}^{(23)} + \sum_{n=-\infty}^{\infty} F_n \zeta_{mn}^{(24)} + \sum_{n=0}^{\infty} L_n \zeta_{mn}^{(25)} + \sum_{n=1}^{\infty} M_n \zeta_{mn}^{(26)} &= \zeta_m^{(2)} \\ \sum_{n=-\infty}^{\infty} A_n \zeta_{mn}^{(31)} + \sum_{n=1}^{\infty} D_n \zeta_{mn}^{(32)} + \sum_{n=1}^{\infty} E_n \zeta_{mn}^{(33)} + \sum_{n=-\infty}^{\infty} F_n \zeta_{mn}^{(34)} + \sum_{n=0}^{\infty} L_n \zeta_{mn}^{(35)} + \sum_{n=1}^{\infty} M_n \zeta_{mn}^{(36)} &= \zeta_m^{(3)} \\ \sum_{n=1}^{\infty} D_n \zeta_{mn}^{(42)} + \sum_{n=1}^{\infty} E_n \zeta_{mn}^{(43)} + \sum_{n=1}^{\infty} L_n \zeta_{mn}^{(45)} + \sum_{n=1}^{\infty} M_n \zeta_{mn}^{(46)} &= \zeta_m^{(4)} \end{aligned} \tag{16}$$

Where,  $\zeta_{mn}^{(11)} = \frac{1}{2\pi} \int_{-\pi}^{\pi} \zeta_n^{(11)} e^{-im\theta} d\theta$ ,  $\zeta_m^{(1)} = \frac{1}{2\pi} \int_{-\pi}^{\pi} \zeta^{(1)} e^{-im\theta} d\theta$ , other equations are the same. Equation (16) is the infinite algebraic equation system for determining unknown constants, which can be solved by using the convergence of cylindrical functions.

## V. DYNAMIC STRESS CONCENTRATION FACTOR AND ELECTRIC FIELD INTENSITY CONCENTRATION FACTOR

The expressions of dynamic stress and electric field intensity around the cylindrical inclusion in right-angle piezoelectric medium can be written as:

$$\begin{aligned}
 \tau_{\theta z}^t &= \tau_{\theta z}^{(ie)} + \tau_{\theta z}^{(re)} + \tau_{\theta z}^{(s)} \\
 &= \frac{ik^M}{2} c_{44}^M (1 + \lambda^M) \cdot \sum_{n=-\infty}^{+\infty} A_n \cdot \left[ \sum_{j=1}^4 \chi_n^{(j)} \exp(i\theta) - \sum_{j=1}^4 \gamma_n^{(j)} \exp(-i\theta) \right] \\
 &+ ie_{15}^M \cdot \sum_{n=1}^{+\infty} D_n \cdot \left[ \sum_{j=1}^2 \zeta_n^{(j)} \exp(i\theta) - \sum_{j=1}^2 \varrho_n^{(j)} \exp(-i\theta) \right] \\
 &+ ie_{15}^M \cdot \sum_{n=1}^{+\infty} E_n \cdot \left[ \sum_{j=1}^2 \upsilon_n^{(j)} \exp(i\theta) - \sum_{j=1}^2 \psi_n^{(j)} \exp(-i\theta) \right] \\
 &- ic_{44}^M (1 + \lambda^M) k^M w_0 [T_1 \sin(\theta - \beta_0) + T_2 \sin(\theta - \alpha_0) + T_3 \sin(\theta + \beta_0) + T_4 \sin(\theta + \alpha_0)]
 \end{aligned} \tag{17}$$

$$\begin{aligned}
 E_{\theta}^t &= -i \left( \frac{\partial \phi^t}{\partial \eta} \cdot e^{i\theta} - \frac{\partial \phi^t}{\partial \bar{\eta}} \cdot e^{-i\theta} \right) \\
 &= -i \left[ \frac{\partial (\phi^{(ie)} + \phi^{(re)} + \phi^{(s)})}{\partial \eta} \cdot e^{i\theta} - \frac{\partial (\phi^{(ie)} + \phi^{(re)} + \phi^{(s)})}{\partial \bar{\eta}} \cdot e^{-i\theta} \right] \\
 &= -\frac{ik^M}{2} \cdot \frac{e_{15}^M}{\kappa_{11}^M} \sum_{n=-\infty}^{+\infty} A_n \cdot \left[ \sum_{j=1}^4 \chi_n^{(j)} \exp(i\theta) - \sum_{j=1}^4 \gamma_n^{(j)} \exp(-i\theta) \right] \\
 &+ i \frac{e_{15}^M}{\kappa_{11}^M} k^M w_0 [T_1 \sin(\theta - \beta_0) + T_2 \sin(\theta - \alpha_0) + T_3 \sin(\theta + \beta_0) + T_4 \sin(\theta + \alpha_0)] \\
 &- i \cdot \sum_{n=1}^{+\infty} D_n \cdot \left[ \sum_{j=1}^2 \zeta_n^{(j)} \exp(i\theta) - \sum_{j=1}^2 \varrho_n^{(j)} \exp(-i\theta) \right] \\
 &- i \cdot \sum_{n=1}^{+\infty} E_n \cdot \left[ \sum_{j=1}^2 \upsilon_n^{(j)} \exp(i\theta) - \sum_{j=1}^2 \psi_n^{(j)} \exp(-i\theta) \right]
 \end{aligned} \tag{18}$$

The dimensionless dynamic stress concentration factor around the inclusion is:

$$\tau^* = \left| \frac{\tau_{\theta z}^t \Big|_{r=R}}{\tau_0} \right| \tag{19}$$

Where  $\tau_0 = c_{44}^M (1 + \lambda^M) k^M w_0$  is the stress amplitude of incident wave in piezoelectric medium.

The dimensionless electric field intensity concentration factor is:

$$E^* = \left| \frac{E_{\theta}^t \Big|_{r=R}}{E_0} \right| \tag{20}$$

Where  $E_0 = \frac{e_{15}^M}{\kappa_{11}^M} (1 + \lambda^M) k^M w_0$  is the electric field intensity amplitude of the incident wave.

## VI. NUMERICAL EXAMPLE AND DISCUSSIONS

As an example, this section gives the calculation results of dynamic stress concentration factor and electric field intensity concentration factor around cylindrical inclusion, and discusses two concentration factors varying with the physical parameters of material and structural geometric parameters.

(1) Figure 3 depicts variations of  $\tau^*$  with the incident angle of the wave when the cylindrical inclusion degenerates to a hole, and the result is in good agreement with reference [18]. Figure 4 shows variations of  $\tau^*$  with the incident angle at the point  $\theta = \pi/2$  around the inclusion. It can be seen that when the wave is incident horizontally or vertically, the value of  $\tau^*$  is the largest, and the value curve is obviously larger when  $k^M R = 1.0$  than the other three curves. In the following simulation examples, it is assumed that the wave is incident horizontally.

(2) Figures 5 and 6 show the change of  $\tau^*$  with  $e_{15}^M / e_{15}^I$ . With the increase of  $e_{15}^M / e_{15}^I$ , the value of  $\tau^*$  hardly changes and its figure is almost symmetrical along the  $X$  axis when  $k^M R = 0.1$ , and the level of  $\tau^*$  decreases under the condition of  $k^M R = 1.0$ . Moreover it can be seen that the value of  $\tau^*$  generally decreases in reverse polarity.

(3) Figures 7 and 8 are demonstrated the variations of  $\tau^*$  with  $\kappa_{11}^M / \kappa_{11}^I$ . It can be seen that the value of  $\tau^*$  hardly change with the decrease of  $\kappa_{11}^M / \kappa_{11}^I$  under the condition of quasi-static  $k^M R = 0.1$ , but it increases slightly when  $k^M R = 1.0$ .

(4) At Figures 9 and 10, the variations of  $\tau^*$  with  $h/R$  are shown. The value of  $\tau^*$  hardly changes with the increase of  $h/R$  in quasi-static  $k^M R = 0.1$ . Under the condition of  $k^M R = 1.0$ , the level of  $\tau^*$  at  $h/R = 3$  is larger than that at  $h/R = 1.5$ . With the further increase of  $h/R$ , the value of  $\tau^*$  decreases slightly, but its value hardly changes after  $h/R = 6$ , which shows that the free surface of the right-angle field has little influence on  $\tau^*$  when reaching a certain distance.

(5) Figures 11 and 12 show the variations of  $\tau^*$  with  $d/R$ . In the case of quasi-static  $k^M R = 0.1$ , the value of  $\tau^*$  increases with the growth of  $d/R$ . When  $k^M R = 1.0$ , the value of  $\tau^*$  fluctuates with

the increase of  $d/R$ , instead of increasing or decreasing blindly, and the position with the most severe dynamic stress concentration also changes correspondingly.

(6) Figures 13 and 14 illustrate the variations of  $\tau^*$  with  $k^M R$  at  $\theta=\pi/2$  around the inclusion. It can be seen from Figure 13 that the value of  $\tau^*$  is almost unchanged with  $e_{15}^M / e_{15}^I$  when  $k^M R < 0.6$ , and its influence begins to appear with the increase of  $k^M R$ . When  $0.7 < k^M R < 1.6$ , the value of  $\tau^*$  is generally smaller in reverse polarity, and it increases slightly with the decrease of  $e_{15}^M / e_{15}^I$ . As can be seen from Figure 14, with the increase of  $\kappa_{11}^M / \kappa_{11}^I$ , the position where the peak value of each dynamic stress concentration factor curve gradually moves to high frequency, and the peak value also increases correspondingly.

(7) Figures 15 and 16 are curves of  $\tau^*$  at  $\theta=\pi/2$  around the inclusion when  $k^M R$  takes different values. It can be seen from Figure 15 that the curve value corresponding to  $k^M R=1.0$  is the largest, and, the value of  $\tau^*$  gradually tends to be stable with the increase of  $h/R$ , which shows that the influence of interface on stress concentration at the defect gradually decreases with the growth of the distance from the interface. Figure 16 shows that with the increase of  $d/R$ , the peak value of  $\tau^*$  changes little, but the appearing frequency of peak value faster with the increase of  $k^M R$ .

(8) Figures 17 and 18 are curves of  $\tau^*$  at  $\theta=\pi/2$  around the inclusion with different values of  $e_{15}^M / e_{15}^I$ . Figure 17 shows that with the growth of  $d/R$ , the peak values of  $\tau^*$  gradually tend to be stable, and the distance between the peaks remains unchanged. Generally, the  $\tau^*$  value in the case of reverse polarity is relatively smaller. Figure 18 depicts that the curve reaches its peak when  $h/R=4$ , and the oscillation of  $\tau^*$  changes with the growth of  $h/R$ . Its value hardly changes after  $h/R=12$  or so. At the same time, we can see that the  $\tau^*$  value in the case of reverse polarity is relatively small. Take the peak values of  $e_{15}^M / e_{15}^I=5$  and  $e_{15}^M / e_{15}^I=-5$  as examples, the peak values of them are 4.784 and 4.385 respectively. The later is 8.34% smaller than the former.

(9) Figures 19 and 20 show the variations of  $E^*$  with  $e_{15}^M / e_{15}^I$ . It can be seen that the value of  $E^*$  is generally smaller in the case of reverse polarity. With the increase of  $e_{15}^M / e_{15}^I$ , the value of  $E^*$  decreases, but the distribution law of electric field intensity around the inclusion is basically unchanged.

(10) Figures 21 and 22 display the variations of  $E^*$  with  $\kappa_{11}^M / \kappa_{11}^I$ . Similar to the trend of the previous two figures, the value of  $E^*$  increases with the decrease of  $\kappa_{11}^M / \kappa_{11}^I$ , but the position of the maximum value is basically unchanged, and the value of  $E^*$  at  $k^M R=1.0$  is larger than that at  $k^M R=0.1$ .

(11) Figures 23 and 24 show the variations of  $E^*$  with  $h/R$ . When  $k^M R=0.1$ , the value of  $E^*$  increases slightly with  $h/R$ , but hardly changes after  $h/R=3$ . Under the condition of  $k^M R=1.0$ , the level of  $E^*$  at  $h/R=3$  is larger than that at  $h/R=1.5$ . With the increase of  $h/R$ , the value of  $E^*$  continues to increase in the upper half of the inclusion and decreases slightly in the lower half, but it hardly changes after  $h/R=6$ .

(12) Figures 25 and 26 show the variations of  $E^*$  with  $d/R$ . Similar to stress concentration, the level of  $E^*$  also increases with the growth of  $d/R$  at  $k^M R=0.1$ . The upper and lower parts of the graph are asymmetrical, and the value in the lower part is slightly larger. The value of  $E^*$  at  $d/R=1.5$  is the largest of the four cases when  $k^M R=1.0$ . With the growth of  $d/R$ , the distribution law of  $E^*$  around the inclusion changes greatly, and the maximum value moves to both sides of the figure.

(13) Figures 27 and 28 show the variations of  $E^*$  with  $k^M R$  at  $\theta=\pi/2$  around the inclusion. As can be seen from Figure 27, the value of  $E^*$  decreases with the increase of  $e_{15}^M / e_{15}^I$  within the range  $k^M R < 1.6$ , but a reverse trend is observed at  $1.6 < k^M R < 3$ . With the increase of  $k^M R$ , there is a similar change rule, and the value of  $E^*$  is still much smaller in reverse polarity. Take  $e_{15}^M / e_{15}^I = 5$  and  $e_{15}^M / e_{15}^I = -5$  as examples, the peak values of them are 1.657 and 0.901 respectively. The later is 83.9% smaller than the former. Figure 28 depicts that with the increase of  $\kappa_{11}^M / \kappa_{11}^I$ , the peak value of  $E^*$  also increases correspondingly, and the position where the curve reaches the peak value gradually moves to high frequency.

(14) Figures 29 and 30 are curves of  $E^*$  when  $k^M R$  takes different values. It is displayed from Figure 29 that, similar to the stress concentration, with the increase of  $h/R$ , the value of  $E^*$  gradually tends to be stable and hardly changes any more. Figure 30 shows that, the peak value of the corresponding curve is the largest when  $k^M R=0.5$ , and the peak value is almost unchanged with the increase of  $d/R$ , but the distance of peak value decreases with the increase of  $k^M R$ .

(15) Figures 31 and 32 are curves of  $E^*$  at  $\theta=\pi/2$  around the inclusion with different values in  $e_{15}^M / e_{15}^I$ . Figure 31 shows that with the growth of  $d/R$ , the peak values of  $E^*$  gradually tend to be stable, and the distance between the peaks also remains unchanged. In the case of the same polarity, the value of  $E^*$  decreases with the growth of  $e_{15}^M / e_{15}^I$ . It can be noticed from Figure 32 that the oscillation of  $E^*$  curve changes with the growth of  $h/R$ , and its level hardly changes after  $h/R=12$  or so. At the same time, the value of  $E^*$  is relatively small in the case of reverse

polarity, which indicates that the electric field intensity concentration around the inclusion can be reduced by reversing the polarity of the inclusion under certain conditions.

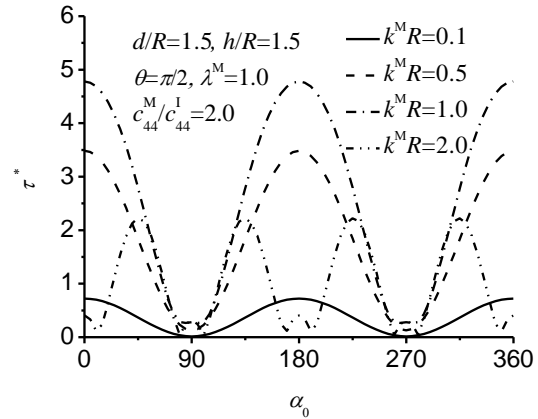
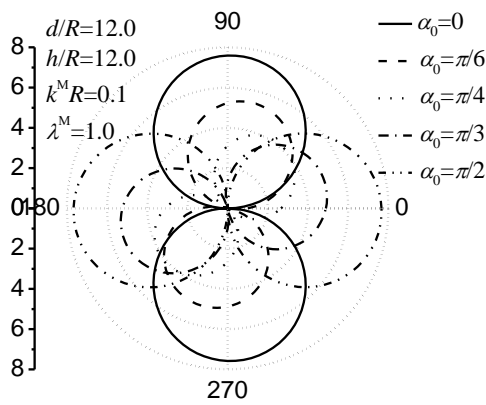


Fig 3: Numerical results of the circular cavity Fig 4: Variation of DSCF vs. incident wave angle

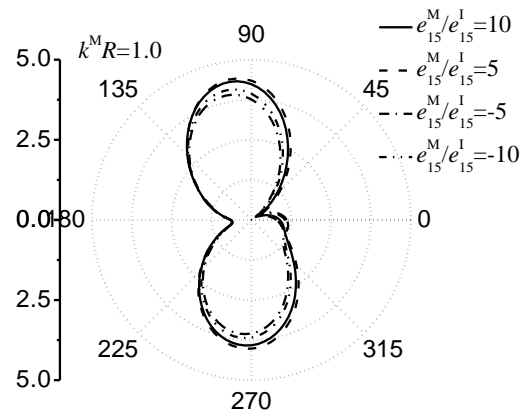
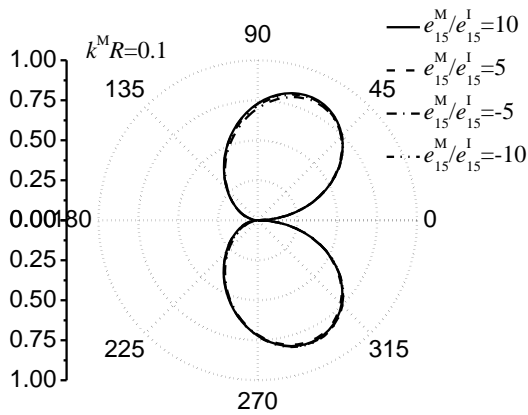


Fig 5: Variation of DSCF vs.  $e_{15}^M / e_{15}^I$  at  $k^M R=0.1$

Fig 6: Variation of DSCF vs.  $e_{15}^M / e_{15}^I$  at  $k^M R=1.0$

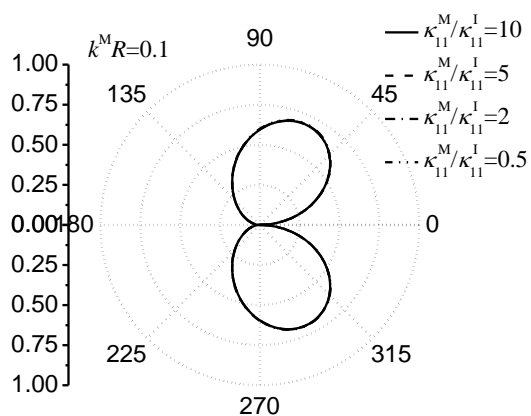


Fig 7: Variation of DSCF vs.  $\kappa_{11}^M / \kappa_{11}^I$  at  $k^M R=0.1$

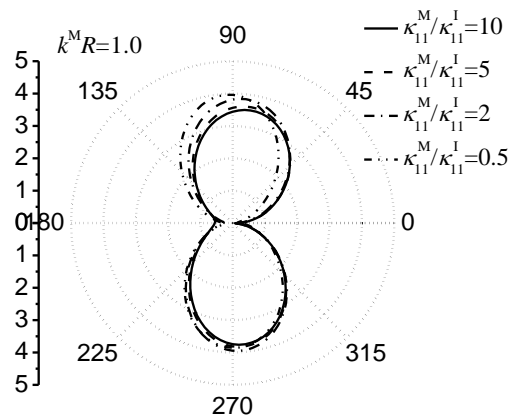


Fig 8: Variation of DSCF vs.  $\kappa_{11}^M / \kappa_{11}^I$  at  $k^M R=1.0$

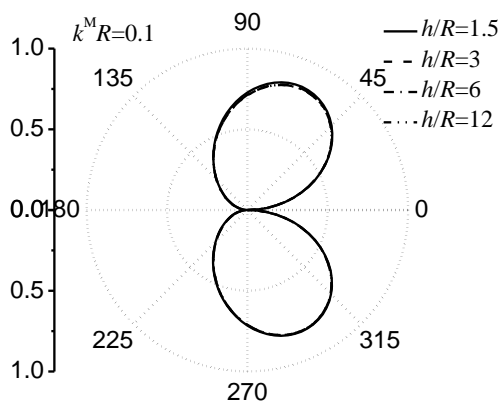


Fig 9: Variation of DSCF vs  $h/R$  at  $k^M R=0.1$

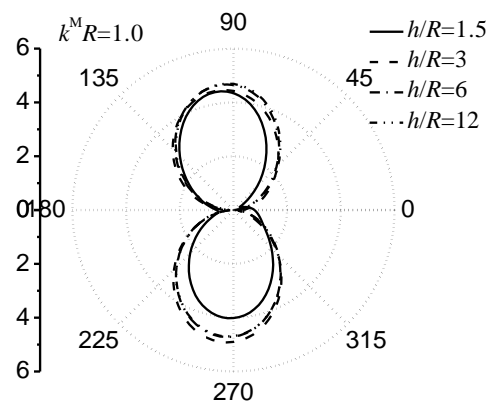


Fig 10: Variation of DSCF vs  $h/R$  at  $k^M R=1.0$

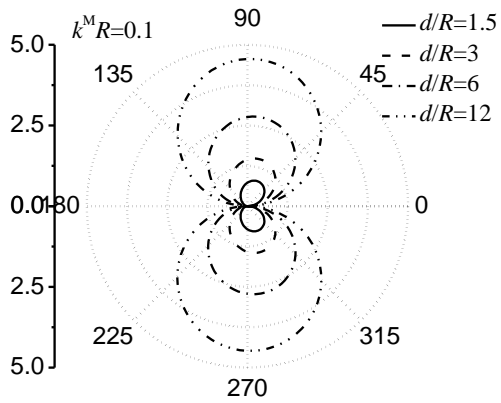


Fig 11: Variation of DSCF vs  $d/R$  at  $k^M R=0.1$

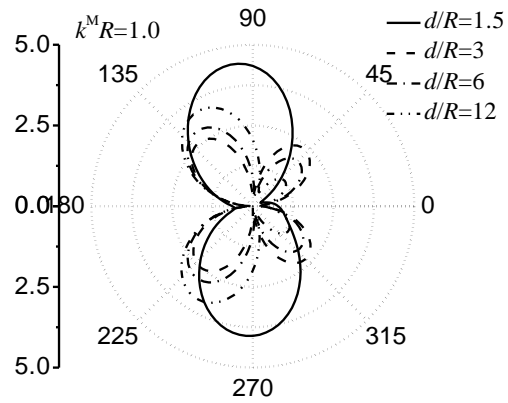


Fig 12: Variation of DSCF vs  $d/R$  at  $k^M R=1.0$

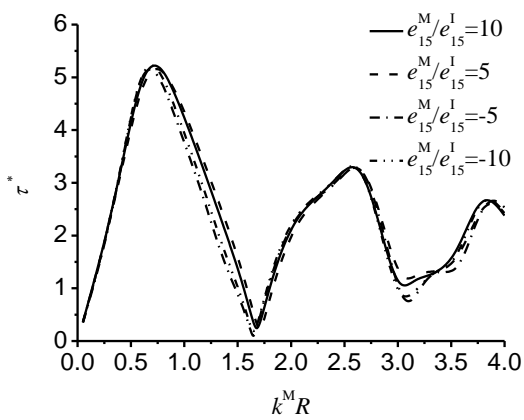


Fig 13: Variation of DSCF vs.  $k^M R$  and  $e_{15}^M / e_{15}^I$

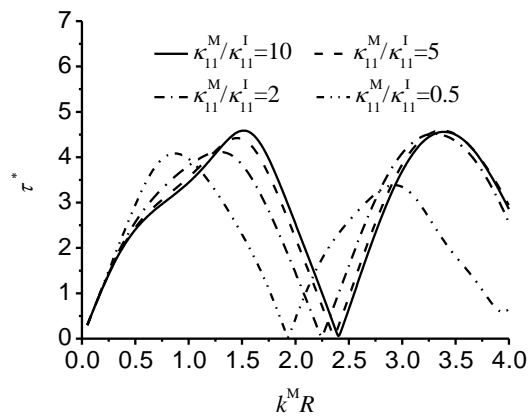


Fig 14: Variation of DSCF vs.  $k^M R$  and  $\kappa_{11}^M / \kappa_{11}^I$

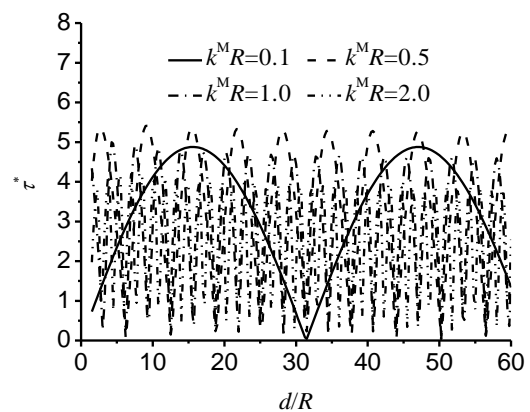
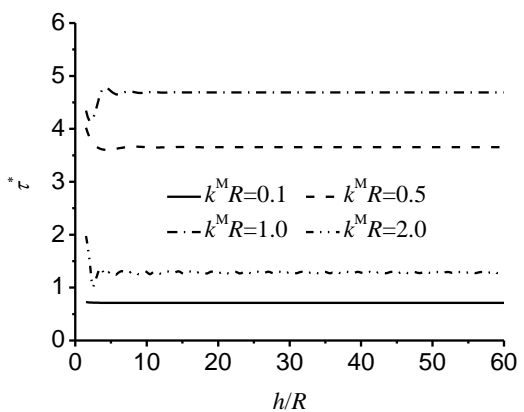


Fig 15: Variation of DSCF vs.  $h/R$  and  $k^M R$

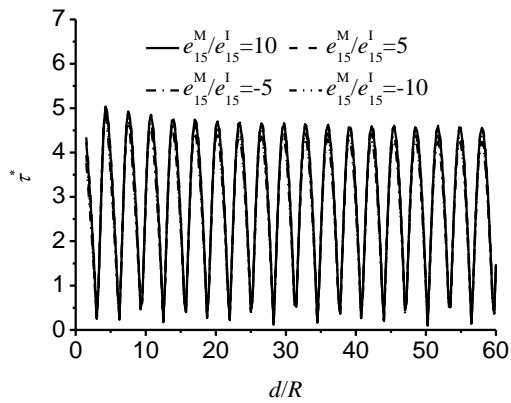


Fig 16: Variation of DSCF vs.  $d/R$  and  $k^M R$

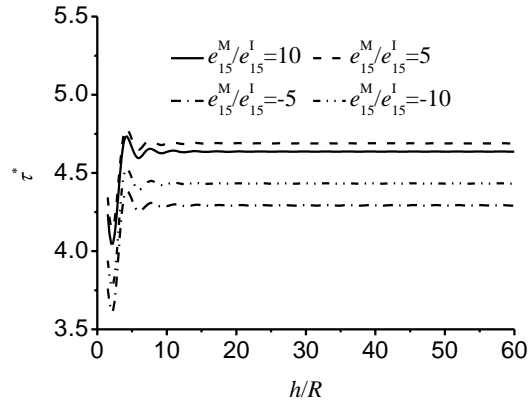


Fig 17: Variation of DSCF vs.  $d/R$  and  $e_{15}^M/e_{15}^I$

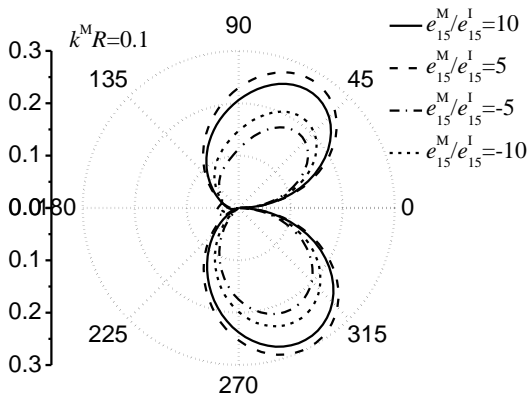


Fig 18: Variation of DSCF vs.  $h/R$  and  $e_{15}^M/e_{15}^I$

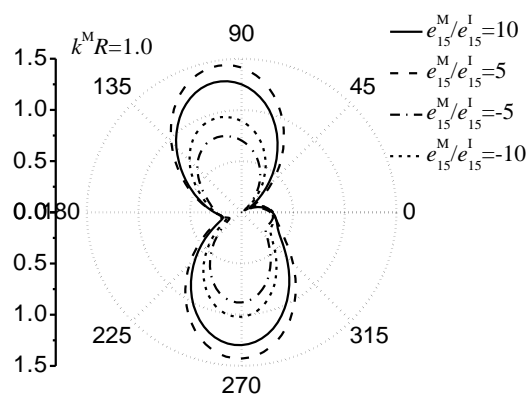


Fig 19: Variation of EFICF vs.  $e_{15}^M/e_{15}^I$  at  $k^M R = 0.1$

Fig 20: Variation of EFICF vs.  $e_{15}^M/e_{15}^I$  at  $k^M R = 1.0$

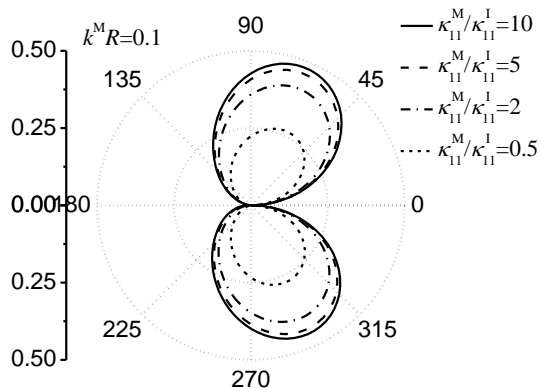


Fig 21: Variation of EFICF vs.  $\kappa_{11}^M / \kappa_{11}^I$  at  $k^M R = 0.1$

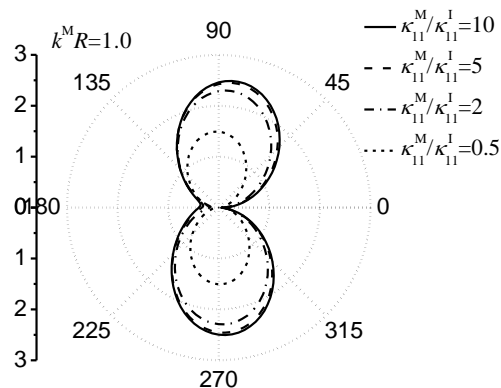


Fig 22: Variation of EFICF vs.  $\kappa_{11}^M / \kappa_{11}^I$  at  $k^M R = 1.0$

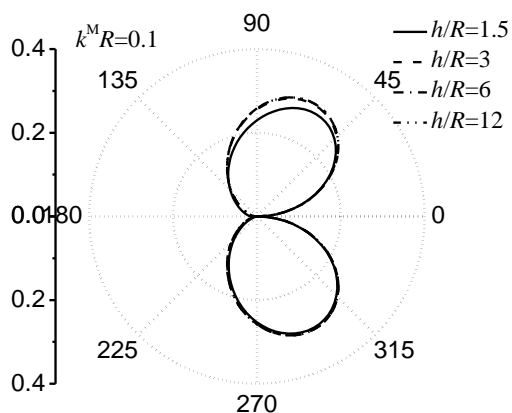


Fig 23: Variation of EFICF vs  $h/R$  at  $k^M R = 0.1$

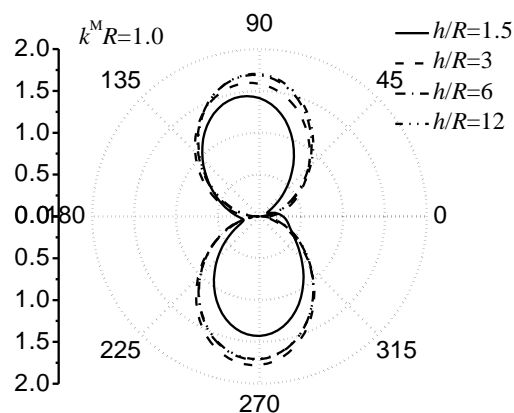


Fig 24: Variation of EFICF vs  $h/R$  at  $k^M R = 1.0$

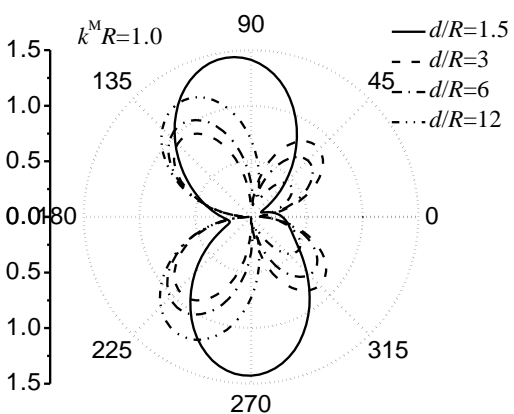
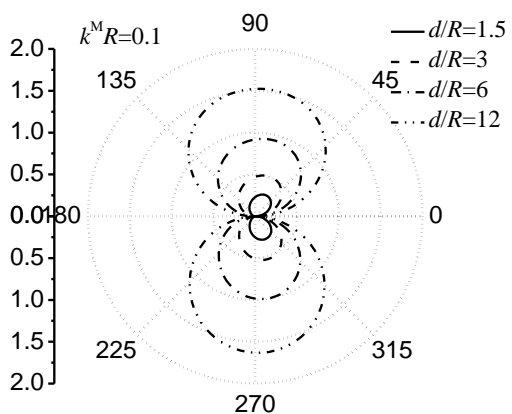


Fig 25: Variation of EFICF vs  $d/R$  at  $k^M R=0.1$

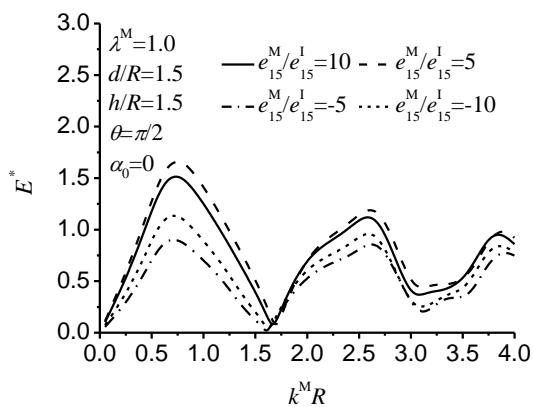


Fig 26: Variation of EFICF vs  $d/R$  at  $k^M R=1.0$

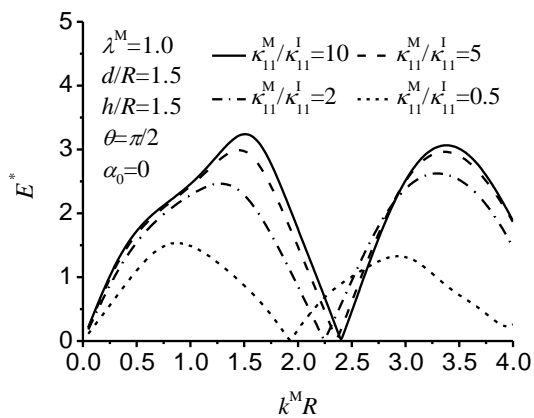


Fig 27: Variation of EFICF vs.  $k^M R$  and  $e_{15}^M / e_{15}^1$

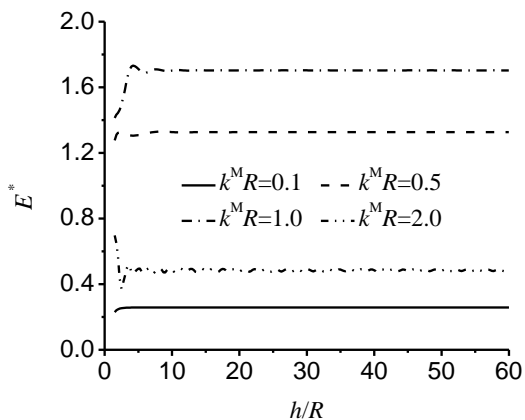


Fig 28: Variation of EFICF vs.  $k^M R$  and  $\kappa_{11}^M / \kappa_{11}^1$

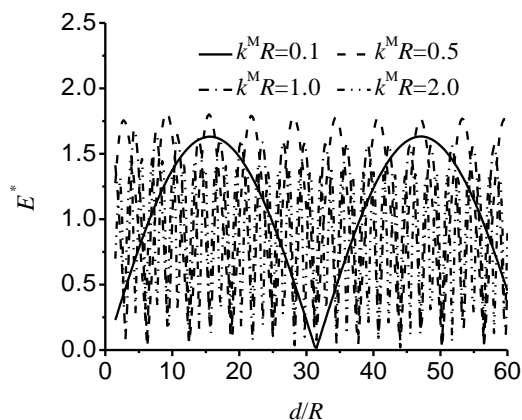


Fig 29: Variation of EFICF vs.  $h/R$  and  $k^M R$

Fig 30: Variation of EFICF vs.  $d/R$  and  $k^M R$

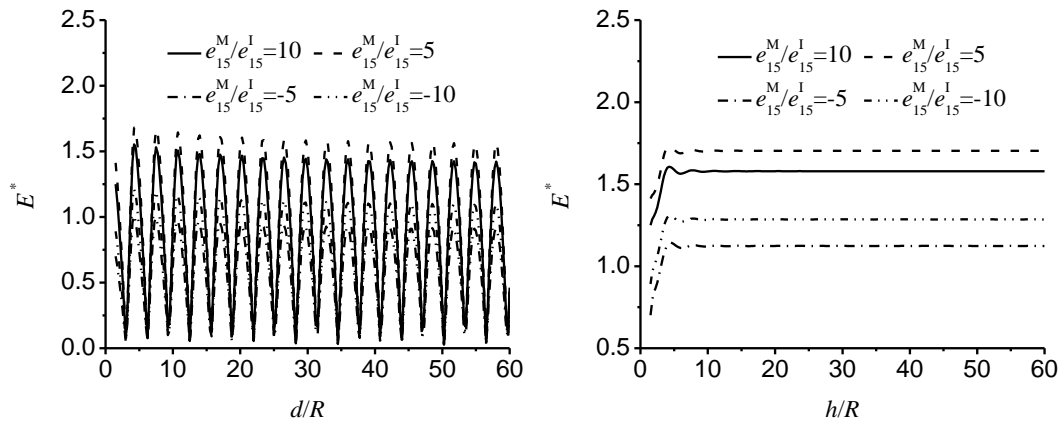


Fig 31: Variation of EFICF vs.  $d/R$  and  $e_{15}^M/e_{15}^I$  Fig 32: Variation of EFICF vs.  $h/R$  and  $e_{15}^M/e_{15}^I$

## VII. CONCLUSIONS

This study provides theoretical derivation of DSCF and EFICF around cylindrical inclusion in right-angle piezoelectric medium by using complex variables, multi-polar coordinate technique and the mirror imaging method. The calculation examples show that with the growth of incident wave frequency, the two concentration factor curves indicate oscillation attenuation, and the peak value appears within the range of  $k^M R = 0.5-1.0$ . The polarity of inclusion is opposite to that of matrix, which can reduce the dynamic stress and electric field intensity concentration around it under certain conditions. With the increase of the distance between the defect and the interface, the influence of the interface on the field concentration around the defect will gradually decrease. Therefore, considering the physical and geometric parameters of material comprehensively, the failure probability of piezoelectric structures in right-angle field can be reduced by selecting the appropriate combination of parameters.

## REFERENCES

- [1] Zhao MH, Wang H, Yang F, Liu T (2006) A magneto-electroelastic medium with an elliptical cavity under combined mechanical-electric-magnetic loading. *Theoretical and Applied Fracture Mechanics* 45, 227-237
- [2] Gao CF, Fan WX (1999) Exact solutions for the plane problem in piezoelectric materials with an elliptic or a crack. *International Journal of Solids and Structures* 25, 2527-2540
- [3] Gao CF (2008) Influence of mechanical stresses on partial discharge in a piezoelectric solid containing cavities. *Engineering Fracture Mechanics* 75, 4920-4924
- [4] Lee KL, Soh AK, Fang DN, et al. (2004) Fracture behavior of inclined elliptical cavities subjected to mixed-mode I and II electro-mechanical loading. *Theoretical and Applied Fracture Mechanics* 41,

125-135

- [5] Sosa H, Khutoryansky N (1996) New Developments Concerning Piezoelectric Materials with Defects. *International Journal of Solids and Structures* 33(23), 3399-3414
- [6] Suzuki T, Sasaki T, Kimura K, Yoshino N (2003) Analyses of isotropic piezoelectric materials with multilayered circular inclusions under out-of-plane shear loadings and their numerical examples. *Nippon Kikai Gakkai Ronbunshu, A Hen/Transactions of the Japan Society of Mechanical Engineers, Part A* 69(3), 579-584
- [7] Suzuki T, Sasaki T, Hirashima K, et al. (2005) Analyses of isotropic piezoelectric materials with multilayered elliptical inclusion under out-of-plane shear loadings. *Acta Mechanica* 179, 211-225
- [8] Chen FM, Shen MH, Hung SY (2006). Circularly cylindrical layered media in antiplane piezoelectricity. *Institute of Physics Publishing* 39, 4250-4256
- [9] Pak YE (2010) Elliptical inclusion problem in antiplane piezoelectricity: Implications for fracture mechanics. *International Journal of Engineering Science* 48, 209-222
- [10] Yang BH, Gao CF, Noda N (2008) Interactions between N circular cylindrical inclusions in a piezoelectric matrix. *Acta Mechanica* 197 (1-2), 31-42
- [11] Meguid SA, Zhong Z (1998) On the elliptical inhomogeneity problem in piezoelectric materials under antiplane shear and inplane electric field. *International Journal of Engineering Science* 36 (3), 329-344
- [12] Hu K, Meguid SA, Wang L. et al. (2021) Electro-elastic field of a piezoelectric quasicrystal medium containing two cylindrical inclusions. *Acta Mechanica* 232, 2513-2533
- [13] Shindo Y, Moribayashi H, Narita F (2002) Scattering of antiplane shear waves by a circular piezoelectric inclusion embedded in a piezoelectric medium subjected to a steady-state electrical load. *ZAMM Zeitschrift fur Angewandte Mathematik und Mechanik* 82 (1), 43-49
- [14] Du JK, Shen YP, Wang X (2002) Scattering of anti-plane shear waves by a partially debonded piezoelectric circular cylindrical inclusion. *Acta Mechanica* 158, 169-182
- [15] Feng W, Wang L, Jiang Z, Zhao Y (2004) Shear wave scattering from a partially debonded piezoelectric cylindrical inclusion. *Acta Mechanica Solida Sinica* 17(3), 258-269
- [16] Bleustein JL (1968) A new surface wave in piezoelectric materials. *Applied Physics letter* 13, 412-413
- [17] Achenbach JD (1973) *Wave propagation in elastic solids*. Amsterdam: North-Holland Publishing Company 110-114.
- [18] Shi Y, Qi H, Yang ZL (2008) Scattering of SH-wave by circular cavity in right-angle plane and seismic ground motion. *Journal of Applied Mechanics* 25(3), 392-397